Contents lists available at ScienceDirect

Computational Materials Science

journal homepage: www.elsevier.com/locate/commatsci

Full length article

Linear-scaling density functional theory (DFT) simulations of point, Frenkel and Schottky defects in CeO$_2$

Nabeel Anwar [a], Robert M. Harker [b], Mark T. Storr [b], Marco Molinari [c], Chris-Kriton Skylaris [a,*]

[a] *School of Chemistry, University of Southampton, Southampton, SO17 1BJ, UK*
[b] *AWE, Aldermaston, Reading, RG7 4PR, UK*
[c] *Department of Chemical Sciences, University of Huddersfield, Huddersfield, HD1 3DH, UK*

ARTICLE INFO

ABSTRACT

CeO$_2$ (ceria) is a material of significant industrial and technological importance, used in solid oxide fuel cells and catalysis. Here, we explore the usage of linear-scaling density functional theory as implemented in the ONETEP code, which allows to use larger simulation cells. By using DFT+U calculations we revise the defect chemistry of ceria, including point defects, Frenkel and Schottky defects.

We found that the ground state of an oxygen vacancy is associated to two neighbouring reduced cerium sites. A cerium vacancy is the least favourable point defect, where holes localise on neighbouring oxygen sites. It is more favourable to displace an oxygen interstitial defect away from the octahedral interstitial site, with the formation of a stable peroxide species. Our simulations show that a cerium interstitial is best accommodated in the octahedral interstitial site, as this minimises the distortion of the lattice.

Placing a vacancy and an interstitial defect at a separation of 5.18 Å for the OF<110> and 4.77 Å for the CeF<111>, stable Frenkel defects can be formed. We also studied the effect of different supercell size on the energetic ordering of Schottky defects, where the S<111> is more favourable than the S<110> for a given simulation cells containing 324 or more atoms.

1. Introduction

CeO$_2$ (ceria) based materials have been studied for their versatility in a range of industrial applications. The oxidation and reduction properties of ceria make it suitable for use in catalysis [1], solid oxide fuel cells (SOFC) [2], and gas sensors [3]. A high thermal stability allows ceria to act as an effective catalyst [4–6], as well as a support for other catalysts [1,7–10]. Stoichiometric ceria is a poor ionic conductor [11], but releasing oxygen under reducing conditions [12–14], ceria forms mobile oxygen vacancies, which increase its ionic conductivity [15–18]. Further enhancements in ionic conductivity can be achieved by introducing dopants [19–28], making it a candidate electrolyte in SOFC, operating in the temperature range of 500–1000 K [29].

Bulk ceria adopts the calcium fluoride (CaF$_2$) crystal structure, with the Fm$\bar{3}$m space group. In this structure, the oxygen occupies tetrahedral holes of the face-centred cubic (FCC) cerium lattice. Each cerium cation coordinates to eight oxygen anions, whereas each O^{2-} anion coordinates to four Ce^{4+} cations. CeO$_2$ is an insulator, with an experimental band gap reported in the range of 2.76 eV to 3.60 eV [30–32], where the 4f-states of Ce^{4+} are completely unoccupied.

Ceria has an identical crystal structure to many actinide oxides (AnO$_2$) such as PuO$_2$, which can be used as a nuclear fuel [33,34]. With comparable bulk properties [35–37] and a similar electronic structure to PuO$_2$ [38], ceria can be used as a reasonable stimulant. Using surrogate materials for PuO$_2$ work can be advantageous as they are less toxic, relatively inexpensive and can be studied in standard laboratories [33,39–41]. In addition, the use of a non-radioactive surrogate such as CeO$_2$ allows us to develop understanding of the chemical effects without the self-irradiation in the PuO$_2$ system.

The ingrowth of radiation induced defects and daughter products changes the composition (and hence physical and mechanical properties) of AnO$_2$ materials over time [39,42]. The predominant decay route for plutonium atoms is through α-decay where a helium nucleus (4.8–5.5 MeV) and the uranium recoil particle (82–94 keV) both create defect damage but over different length scales. The α-particle has a range of the order of 10 μm in oxide, losing its energy by electronic stopping; defects produced are largely isolated Frenkel pairs with little annihilation or clustering of the defects [43].

A number of computational studies have explored the bulk properties of ceria [35,36,44–46], the formation of defects and their interactions within the material [16,28,42,47–49]. However, the unfavourable, cubic-scaling of conventional density functional theory

---

* Corresponding author.

E-mail addresses: c.skylaris@soton.ac.uk, N.Anwar@soton.ac.uk (C.-K. Skylaris).

(DFT) methods, limit these studies to small supercells. Small simulation cells introduce finite-size effects, arising from the long-range electrostatic interactions between a charged defect and its periodic images [50–52]. These effects are accounted for by corrections schemes such as Makov-Payne [53] and Freysoldt, Neugebauer and Van de Walle (FNV) [54]. These schemes aim to alleviate the need for simulations with prohibitively large supercells in order to minimise finite-size effects.

An alternative approach is to use linear-scaling DFT methods, which reduce the unfavourable, cubic scaling of conventional DFT with increasing system size. To achieve linear-scaling, ONETEP (order-N electronic total energy package) [55] uses a reformulation of DFT, based on the one-particle density matrix, $\rho(\mathbf{r}, \mathbf{r}')$. ONETEP exploits the locality or nearsightedness of the density matrix [56,57] by expanding the Kohn–Sham orbitals as a linear combination of non-orthogonal generalised Wannier functions (NGWFs) [58]. These spatially localised orbitals are self-consistently optimised during the energy minimisation. Once the system size reaches or exceeds a critical number of atoms (crossover point), linear-scaling DFT methods are more efficient than conventional DFT. The crossover point is system dependent and generally lies on the order of hundreds of atoms [59].

Investigations into defects in materials containing f-block elements with conventional DFT methods are limited to 96 atoms simulation cells. Due to the unfavourable time scaling of conventional DFT, there are few studies using simulation cells approaching thousands of atoms size [60]. Instead some studies have used semi-empirical interatomic potentials to perform large simulations, but the quality of the predictive capability can be dependent upon the data used in the fitting process [37,60–62]. We expand the simulation cell up to 1500 atoms to study a range of point defects, Frenkel and Schottky defects using the ONETEP linear-scaling DFT code. By increasing the supercell size, we can isolate and dilute the concentration of point defects to minimise finite-size effects. For the complex defects such as Frenkel defects we considered the impact of placing the interstitial atom in different chemical environments has on the defect formation energy.

2. Methodology

2.1. Computational details

Cell optimisations of stoichiometric ceria were performed using the CASTEP plane-wave DFT package [63]. Calculations were performed using the Perdew–Burke–Ernzerhof (PBE) [64] generalised gradient approximation (GGA) exchange–correlation functional. The valence electrons for cerium $(5s^2 5p^6 4f^1 6s^2 5d^1)$ and oxygen $(2s^2 2p^4)$ were treated using a plane-wave basis set, with a kinetic energy cut-off of 800 eV, whereas the core electrons were frozen in the norm-conserving pseudopotential (NCP) on-the-fly generated (OTFG) by CASTEP. A $4 \times 4 \times 4$ Monkhorst–Pack k-points mesh [65] was used to sample the Brillouin zone of the simulation cells optimised with CASTEP.

The system is considered as spin polarised, and spin–orbit coupling is not included. Self consistent electronic minimisation were performed with ensemble density functional theory (EDFT) [66,67], where the Fermi-Dirac smearing scheme with an electronic temperature of 1000 K was applied. The electronic energies were converged to 1×10^{-5} eV, and structural relaxation were conducted until the forces acting on each atom were below 0.05 eV Å^{-1}.

The on-site Coulomb repulsion was accounted for by applying the Hubbard parameter, U to favour localisation of electronic states. A rotational invariant approach [67] is used with an effective U parameter of 5.0 eV, based upon the available literature [16,28,44,48,68–72]. Some studies also include a U parameter of 5.5 eV for the O $2p$-states, although this has limited impact on the point defect formation energies [47]. Ramping U is also less appropriate as it can affect the orbital orderings [73]. Using a U correction may give rise to metastable states, which have been studied with the occupation matrix control

(OMC) scheme [74–76]. The OMC scheme was not applied in this work, as the $4f$-states of Ce^{4+} are empty in stoichiometric CeO$_2$ and to reduce the required computational resources.

Recognising the computational overheads of plane-wave calculations, we limited our simulations with CASTEP to the $2 \times 2 \times 2$ supercell of the 12 atom unit cell, corresponding to the 96 atom cell. Calculations with larger simulation cells performed using ONETEP, used the same exchange–correlation functional, kinetic energy cut-off energy and OTFG NCP. The electronic energy minimisations with EDFT at 1000 K, are converged to 3×10^{-5} eV and structural relaxations converged to within 0.10 eV Å^{-1} per atom.

A sufficiently large spatial cut-off for the NGWFs of each valence state is chosen at radius of 10.0 a_0. The NGWFs are expanded in the basis of periodic sinc (psinc) functions, which are mathematically equivalent and similar in accuracy to the plane-wave basis [58,77]. A kinetic energy cut-off of 800 eV was sufficient to give a complete description of basis set. The oxygen valence states in ONETEP were assigned 4 NGWFs which correspond to 1 NGWF for the $2s$-orbital and the remaining 3 NGWFs assigned to $2p$-orbitals. The cerium valence states are represented by 17 NGWFs, where the $5s$ and $6s$-orbitals are represented by 1 NGWF each, the $5p$-orbitals by 3 NGWFs, the $4f$-orbitals by 7 NGWFs and the $5d$-orbitals by the remaining 5 NGWFs.

2.2. Defect formation

Firstly, CASTEP was used to optimise a stoichiometric CeO$_2$ simulation cell. Then, point defects were introduced to the cell. The simulation cells were kept neutral, with no addition or removal of electrons. The defective structures were optimised at constant volume, using the lattice parameters of the relaxed, perfect cell. Larger supercells were created from the optimised $2 \times 2 \times 2$ supercell of ceria. Fixed cell optimisations using ONETEP were performed on these larger supercells, in addition to the 96 atom supercell. Charged point defects were introduced to the resulting, stoichiometric structures and then optimised.

The energy required to form a point defect in perfectly crystalline ceria is calculated according to the Zhang-Northrup formula [78,79],

$$E_{\text{defect}}^{\text{form}}(X^q) = E_{\text{defect}}(X^q) - E_{\text{stoich}}(\text{CeO}_2) - \sum_i n_i E_i + q\mu_e, \quad (1)$$

where X is the type of defect and q, its charge state. The total energy of the material containing the defect is denoted as $E_{\text{defect}}(X^q)$ and the total energy for the stoichiometric material is given by $E_{\text{stoich}}(\text{CeO}_2)$. To form a defect in the perfect crystal, n_i number of species i are either removed to form a vacancy ($n_i < 0$) or added to an interstitial site ($n_i > 0$). The change in energy from the addition or removal of atoms is given by E_i of each species. The energy for oxygen is calculated by optimising an O$_2$ molecule in the gas phase,

$$E_{\text{O}} = \frac{1}{2} E_{\text{molecule}}(\text{O}_2) \quad (2)$$

The energy for cerium is calculated by optimising $n = 32$ (CASTEP) and 108 (ONETEP) atoms of bulk cerium metal with an effective U of 5.0 eV applied,

$$E_{\text{Ce}} = \frac{E_{\text{bulk}}(\text{Ce})}{n} \quad (3)$$

The final term is the chemical potential of the electrons, μ_e, which is the Fermi energy, E_{Fermi}.

We introduced Frenkel defects into the simulation cell by removing an atom from a lattice site and placing it in an interstitial position in the stoichiometric simulation cell. The defect formation energies of the Frenkel defects are presented per point defect,

$$E_{\text{Frenkel}}^{\text{form}} = \frac{E_{\text{defect}} - E_{\text{stoich}}}{2} \quad (4)$$

Table 1

Bulk properties of ceria calculated using DFT+U with CASTEP and the comparison with experimental and computational literature.

Bulk properties	CASTEP	Experimental literature	Computational literature
Lattice constant, a (Å)	5.50	5.41[n]	5.494,[a] 5.49[f,o]
Band gap, E_g (eV)	2.70	3.0,[b] 3.0,[c] 2.76,[h] 3.31,[i] 3.60[j]	2.45,[a] 2.50,[g] 2.29[o]
Bulk modulus, B_{VRH} (GPa)	185	204,[d] 220[n]	181,[k] 182,[g] 184[k]
EOS bulk modulus, B (GPa)	185	187[n]	185[f]
EOS B'	4.22	4.85[n]	4.2[j]
Shear modulus, G_{VRH} (GPa)	81	96[d]	82[l]
Young's modulus, E (GPa)	212	249[d]	213[l]
Poisson's ratio, ν	0.32	0.30[d]	0.31[l]
C_{11} (GPa)	351	403,[d] 450[e]	344,[g] 354[m]
C_{12} (GPa)	101	105,[d] 117[e]	101,[g] 102[m]
C_{44} (GPa)	51	60,[d] 57[e]	54,[g] 53[m]
$C_{11} - C_{12}$ (GPa)	250	298,[d] 333[e]	243,[g] 252[m]
$C_{11} + 2C_{12}$ (GPa)	553	613,[d] 684[e]	546,[g] 558[m]

[a]Ref. [47]. [b]Ref. [81]. [c]Ref. [82]. [d]Ref. [83]. [e]Ref. [84]. [f]Ref. [42]. [g]Ref. [49]. [h]Ref. [30]. [i]Ref. [85]. [j]Ref. [32]. [k]Ref. [48]. [l]Ref. [36]. [m]Ref. [86]. [n]Ref. [87]. [o]Ref. [88].

The Schottky defect was created by the removal of a neutral, formula unit of CeO$_2$ from the stoichiometric material. The defect formation energy for the Schottky defect is given per point defect,

$$E_{Schottky}^{form} = \frac{1}{3}\left(E_{defect} - E_{stoich} + \frac{E_{stoich}}{x}\right) \tag{5}$$

where x is number of formula units in the supercell. In general the formation energy is positive, as it costs energy to create a defect.

3. Results & discussion

3.1. Bulk properties of stoichiometric CeO$_2$

A summary of the bulk properties calculated from a 12 atom CASTEP simulation cell of stoichiometric, bulk ceria is given in Table 1. Cell optimisation of bulk ceria yields a lattice constant that is consistent with the computational literature, but larger than the experimentally determined value. This difference is attributed to the overestimation of the structure parameter by the GGA functional, which is exacerbated by the inclusion of the Hubbard, U correction. The U correction of 5.0 eV, ensures that a sufficient band gap is created of 2.70 eV as shown in Figure 3 of the supplementary material, which is closer to the reported experimental range of 2.76 eV to 3.60 eV. GGA functionals provide accurate ground state properties, although they are known to underestimate band gaps [80].

We determined the mechanical properties of bulk ceria in Table 1, by applying the appropriate strain pattern to the optimised simulation cell [89], using the Voigt–Reuss–Hill (VRH) approximation [90]. To assess the mechanical stability of this cubic crystal, the elastic constants were compared with the Born-stability criteria [91] given by Eq. (6),

$$\begin{cases} C_{11} > 0; \quad C_{44} > 0 \\ C_{11} - C_{12} > 0 \\ C_{11} + 2C_{12} > 0 \end{cases} \tag{6}$$

As can be seen, the calculated elastic constants satisfy the stability criteria.

The calculated elastic constants, C_{11}, C_{12} and C_{44} from this study sit, in general, within the range of reported computational values and are lower value as compared to experiment. For example, our calculated elastic constant is 13%–22% below the experimentally determined values for C_{11}, some 4%–14% below for C_{12} and 11%–15% below for C_{44}. This lower value is, however, typical of computational studies as can be observed in Table 1. This is often attributed to temperature and volume effects [35] which are not accounted for by our DFT simulations and the approximations of the exchange–correlation functional.

Bulk and shear moduli calculated from the Voigt–Reuss–Hill (VRH) approximation (B_{VRH} at 185 GPa and G_{VRH} at 81 GPa respectively) are again close to other comparable computational literature references

but are lower than that observed in experiment (9%–16% and 16% respectively). We calculated ν from our determined E and B, where we find good agreement with both computational and experimental literature. We also calculated the bulk modulus by fitting the third-order Birch-Murnaghan equation of state (EOS), for different cell volumes shown in Figure 4 of the supplementary material. Fitting the cubic polynomial to the free energy-volume plot, the minimum bulk modulus at minimum volume, B_0 is found to be 1.15 eV/Å^3 or 185 GPa. The first derivative of B_0 with respect to pressure at constant temperature is the dimensionless parameter B_0', with a value of 4.22, which is typical for this material [36,42]. This result is consistent with our bulk modulus obtained with the VRH approximation. The smaller calculated bulk modulus, when compared to experiment, is typically attributed to the chosen exchange–correlation functional.

### 3.2. Structure and electronic properties of point defects

Oxygen vacancy formation in ceria involves two excess electrons localising onto adjacent cerium sites, which reduces the cerium ions from Ce(IV) to Ce(III). The process is illustrated by the Kröger-Vink notation,

$$O_O^\times + 2Ce_{Ce}^\times \rightarrow V_O^{\bullet\bullet} + 2Ce_{Ce}' + \frac{1}{2}O_2(g) \tag{7}$$
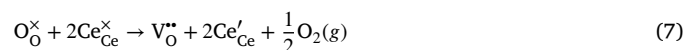
where $O_O^\times$ and $Ce_{Ce}^\times$ represent the oxygen and cerium atoms on their respective lattice sites. $V_O^{\bullet\bullet}$ is the doubly positively charged oxygen vacancy and Ce_{Ce}' is the singly negatively charged cerium in the lattice. Fig. 1(a) shows that this region of effective positive charge attracts the first nearest neighbour oxygen ions, which move off their lattice site towards the vacant site. Mulliken population analysis reveals that in ONETEP, two electrons localise onto one adjacent cerium ion each, finding a stable ground state. The localisation of the electrons was aided by the self-consistent optimisation of the spatially localised valence orbitals (NGWFs) during the geometry relaxation [92].

In CASTEP, the two electrons localise across four cerium sites, which suggests the presence of a metastable state. All our attempts to localise the two electrons onto two cerium sites failed, which been has shown by several studies using plane-wave DFT [48,49,93]. The local structure around the vacant site was distorted by replacing the cerium sites coordinated with the oxygen atom with lanthanum atoms. The resulting structure was then relaxed with the lanthanum sites reverted back to cerium, however this was unsuccessful in localising the two electrons.

The projected density of states (PDOS) plotted with Sumo [94] in Fig. 1(a) shows that excess electrons occupy the empty $4f$-states on the neighbouring cerium ions. Experimental [12,81,95] and previous theoretical [47] studies both support the presence of an additional peak for the defective material. The peak appears in the band gap, between the oxygen $2p$-state dominated valence band and the conduction band containing the cerium $4f$-states. This peak indicates the reduction of Ce(IV) to Ce(III).
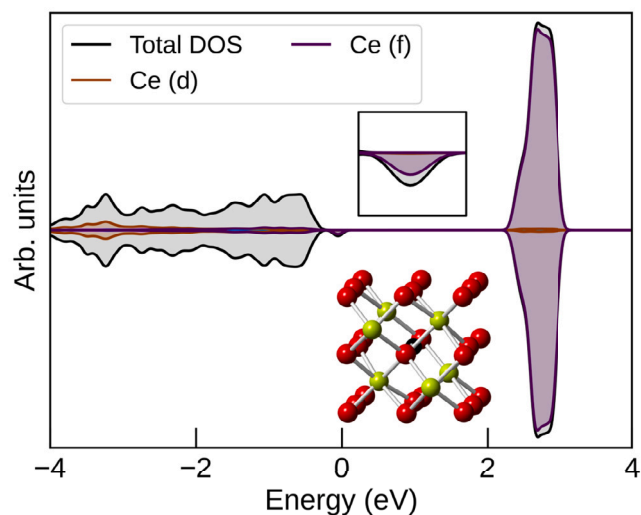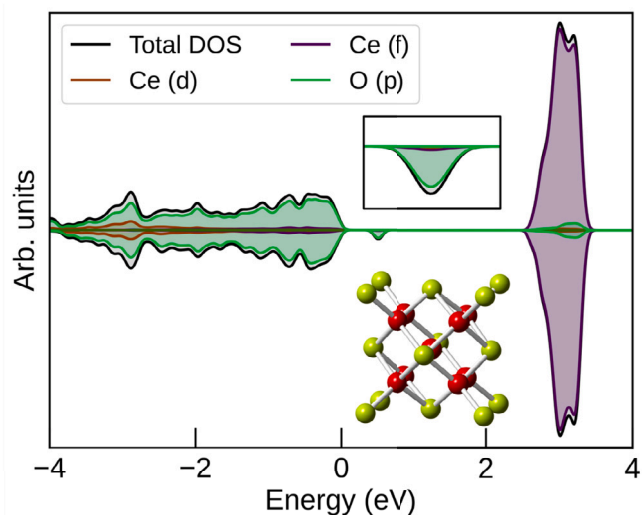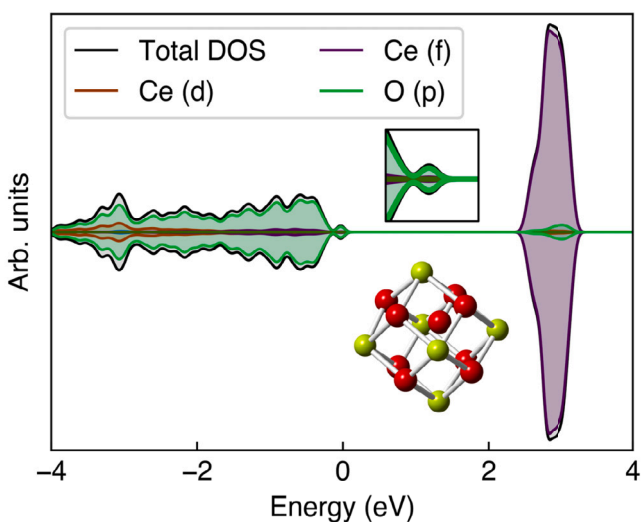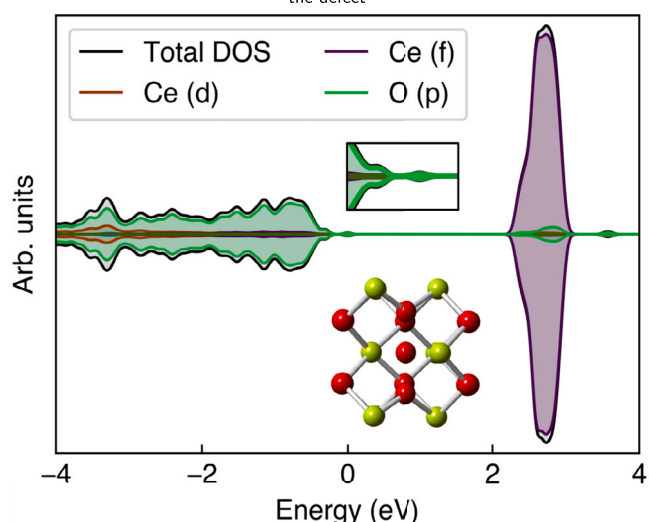
Fig. 1. Local structure around the (a) oxygen vacancy, (b) interstitial oxygen (octahedral), (c) peroxide and (d) interstitial oxygen (oxygen edge) defects in ceria and their respective PDOS plots for the 96 atom simulation cell from ONETEP. The oxygen atoms are given in red, cerium atoms in yellow and the oxygen vacancy in black. The DOS plot is decomposed into the O-p (p), Ce-d (d) and Ce-f (f) states.

Using ONETEP, introducing an oxygen into an octahedral interstitial site, produces localised holes on the interstitial ion, O_i' and neighbouring oxygen ions, $O_O^{\bullet}$,

$$O_O^x + \frac{1}{2}O_2(g) \rightarrow O_i' + O_O^{\bullet} \tag{8}$$

Fig. 1(b) shows an oxygen atom placed in an octahedral interstitial lattice site. The work by Keating et al. suggests that this position is less favourable [47], instead showing the formation of the peroxide species. No such species was found in either our ONETEP or CASTEP optimisations, where the interstitial oxygen remains in the octahedral site. In both calculations, the first nearest neighbour oxygen atoms move off their lattice sites, away from the interstitial ion. Fig. 1(c) shows that by placing the interstitial oxygen approximately 1.0 Å from an oxygen atom of the lattice, we were able to form the peroxide species,

$$O_O^x + \frac{1}{2}O_2(g) \rightarrow (O_2)_O^x \tag{9}$$

The PDOS contains a new peak in the band gap, which corresponds the formation of the peroxide species. Both the CASTEP and ONETEP

Mulliken charges indicate that no holes localised onto neighbouring oxygen sites.

CASTEP charge analysis, placing the interstitial oxygen in the octahedral site or close to the oxygen lattice sites, leads to localisation of two electrons across several and two oxygen lattice sites respectively as shown by the equation,

$$2O_O^x + \frac{1}{2}O_2(g) \rightarrow O_i'' + 2O_O^{\bullet} \tag{10}$$
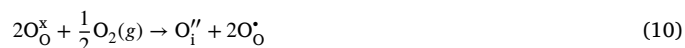
Population analysis shows that this state in ONETEP is only found when placing the interstitial oxygen close to the oxygen lattice sites. The localised holes on the neighbouring oxygen atoms are observed in the PDOS in Fig. 1(d), with a peak in the band gap, assigned to the oxygen 2p-state.

Creating a cerium vacancy, removes four electrons from the lattice, creating holes on the neighbouring oxygen atoms,

$$Ce_{Ce}^x + 4O_O^x \rightarrow V_{Ce}'''' + 4O_O^{\bullet} + Ce(s) \tag{11}$$

The PDOS in Fig. 2(a) for the cerium vacancy indicates the holes are localised onto the oxygen 2p-states, close to the valance band. From the population analysis, the holes localise across eight neighbouring oxygen

Table 2
Formation energies for the oxygen and cerium point defects calculated using DFT+U for stoichiometric ceria and comparison to the computational literature.

Defect	CASTEP (eV)	ONETEP (eV)				Computational literature (eV)	
	96 atom	96 atom	324 atom	768 atom	1500 atom	Stoichiometric	O-rich
$V_O^{\bullet\bullet}$	2.62	2.30	2.49	2.10	2.46	1.56,[a] 3.10,[b] 3.39[c]	2.90,[a] 2.60,[d] 2.80,[e] 4.30,[f] 4.61,[g] 4.57,[h] 4.70[i]
O_i' (octahedral)	–	2.46	3.43	3.19	3.15	–	3.60,[e] 5.14,[g] 4.04[h]
O_i'' (oxygen edge)	2.77	2.09	–	–	–	–	–
O_i'' (octahedral)	2.96	–	–	–	–	2.95[a]	1.60,[a] 4.41,[e] 7.87,[g] 7.72[h]
$(O_2)_O^x$ (peroxide)	1.82	1.26	–	–	–	–	1.73[d]
V_{Ce}''''	14.30	13.58	14.53	14.07	14.67	4.94,[a] 16.59[b]	2.23,[a] 6.29,[d] 7.39,[e] 16.01,[g] 16.60[h]
$Ce_i^{\bullet\bullet\bullet}$ (oxygen edge)	6.99	–	–	–	–	–	–
$Ce_i^{\bullet\bullet\bullet\bullet}$ (oxygen edge)	–	6.45	–	–	–	–	–
$Ce_i^{\bullet\bullet\bullet}$ (octahedral)	1.14	–	2.31	–	2.71	–	10.02,[d] 6.50,[e] 15.41,[g] 14.68[h]
$Ce_i^{\bullet\bullet\bullet\bullet}$ (octahedral)	–	0.62	–	4.52	–	7.68[a]	10.39,[a] 5.06,[e] 16.94,[g] 16.63[h]

[a]Ref. [49]. [b]Ref. [93]. [c]Ref. [16]. [d]Ref. [47]. [e]Ref. [48]. [f]Ref. [88] (PBE+U). [g]Ref. [88] (QM/MM PBE0). [h]Ref. [88] (Mott-Littleton (M-L)). [i]Ref. [96].

sites, as reported by Keating et al. [47]. Fig. 2(a) shows that the nearest neighbour oxygen atoms move away from the negative effective charge of the vacant site. A more pronounced shift of the lattice oxygen ions is reported by Keating et al. when applying a Hubbard U correction of 5.5 eV to the O 2p-states [47].

Placing an interstitial cerium ion in an interstitial lattice site, adds four extra electrons into the system. These additional electrons localise onto a neighbouring cerium lattice sites, reducing them from Ce(IV) to Ce(III),

$$4Ce_{Ce}^x + Ce\,(s) \rightarrow 4Ce_{Ce}' + Ce_i^{\bullet\bullet\bullet\bullet} \tag{12}$$

Alternatively, one electron may remain on the interstitial cerium, with three of the neighbouring cerium lattice sites being reduced to Ce(III),

$$3Ce_{Ce}^x + Ce\,(s) \rightarrow 3Ce_{Ce}' + Ce_i^{\bullet\bullet\bullet} \tag{13}$$

The population analysis from our calculations support the localisation of up to four electrons across four adjacent cerium atoms in the lattice. Several, small peaks appear in the band gap of the PDOS shown in Figs. 2(b) and 2(c), where the peak closest to the valence band is likely the oxidised interstitial cerium ion [47]. The remaining peaks are attributed to the reduction of the lattice cerium atoms from Ce(IV) to Ce(III). For the smallest ONETEP simulation cell, all four electrons localise onto neighbouring cerium sites, whereas in CASTEP this only occurs when the interstitial cerium is placed on the oxygen edge, between two oxygen atoms. Depending on the simulation size, three or four electrons are localised across four adjacent cerium lattice sites.

Fig. 2(b) shows that introducing the interstitial cerium into the octahedral site leads to minimal distortion of the ceria lattice. The oxygen ions remain on their lattice sites while the adjacent cerium ions relax away from the interstitial cerium. Fig. 2(c) shows that placing the interstitial cerium between two lattice oxygen ions also shifts the neighbouring oxygen atoms. The oxygen atoms lying in the same plane as the interstitial cerium, move away from their site to accommodate it. Oxygen atoms lying in adjacent planes move towards the net positively charged interstitial site.

3.3. The energetics of defects

3.3.1. Point defect formation

The defect formation energies were obtained using both CASTEP and ONETEP at different simulation cell sizes and are presented alongside the literature values in Table 2. We make comparisons against the reported formation energies for the stoichiometric condition where possible. The formation energies for the O-rich condition are also included, where the chemical potential of cerium and oxygen are dependent on the stoichiometry of ceria and the partial pressure of oxygen.

We focused on calculating the formation energies of point defects in stoichiometric ceria at increasingly dilute defect concentrations.

Depending on the simulation package and cell size we find different electronic states for the interstitial defects, which contribute to the changing formation energies. In general, our calculations predict that the oxygen vacancy defect is more favourable than oxygen interstitial defect. We found that placing the interstitial oxygen along the oxygen edge gives lower formation energies. The most stable oxygen species was found by forming the peroxide as shown by Keating et al. [47], where they suggest that oxygen species in the octahedral are less stable.

Our formation energies for the cerium defects show greater deviation from the literature. The cerium vacancy defect energies are two to three times greater formation energies than the majority of the literature, with the only comparable value presented in the study by Vanpoucke et al. [93]. The study by Catlow et al. [88] using QM/MM and hybrid exchange–correlation functionals also gave more comparable defect energies to this work. Placing the cerium interstitial along an oxygen edge gives formation energies more comparable to the literature. Inserting the cerium into the octahedral site we find smaller formations energies as this position can better accommodate the interstitial cerium.

Our ONETEP calculations of the point defect energies, in general, show a fluctuation of energies as the supercell size increases (see Figures 9–11 in Supplementary Information): the supercells made up of an odd number of unit cells (3 × 3 × 3, 324 atoms and 5 × 5 × 5, 1500 atoms) are greater in energy than the supercells made up of an even number of unit cells (2 × 2 × 2, 96 atoms and 4 × 4 × 4, 768 atoms). Interestingly the exception to this is the cerium interstitial calculations which do not show this behaviour. Other studies in the literature which use larger simulation cells have reported fluctuating formation energies as a function of simulation cell size, varying by as much as several eV [97,98]. In our case we show a smaller variation for a given charged point defect when compared to examples in the literature [54,97–99]. We cannot definitively identify the source of this behaviour, but several possibilities exist. The fact that we show specific fluctuations with odd numbers of unit cells being higher in energy than the even numbers of unit cells suggest that symmetry effects may be a cause. Certainly, it has been reported that the symmetry around the relaxed defect structures can change with increasing supercell size, with smaller cells favouring more symmetric distortions [97–99]. In addition to this symmetry effect electronic effects also contribute to changing behaviour with increasing supercell size: several plane-wave DFT studies have shown that distortions around the defect site become weaker as the simulation cell size grows [97–100].

The formation energies for the oxygen and cerium vacancy change for increasing simulation sizes in part is due to different degree of relaxation around the defect site. Creating a vacancy removes 1.56% of oxygen and 3.13% of cerium atoms in the 96 atom supercell. Increasing the simulation size to 1500 atoms dilutes the concentration of vacancies to 0.10% for oxygen and 0.20% for cerium. The nearest neighbour oxygen atoms distort from their initial lattice sites towards the oxygen vacancy by up to 0.31 Å in the 96 atom cell. The distortion of the
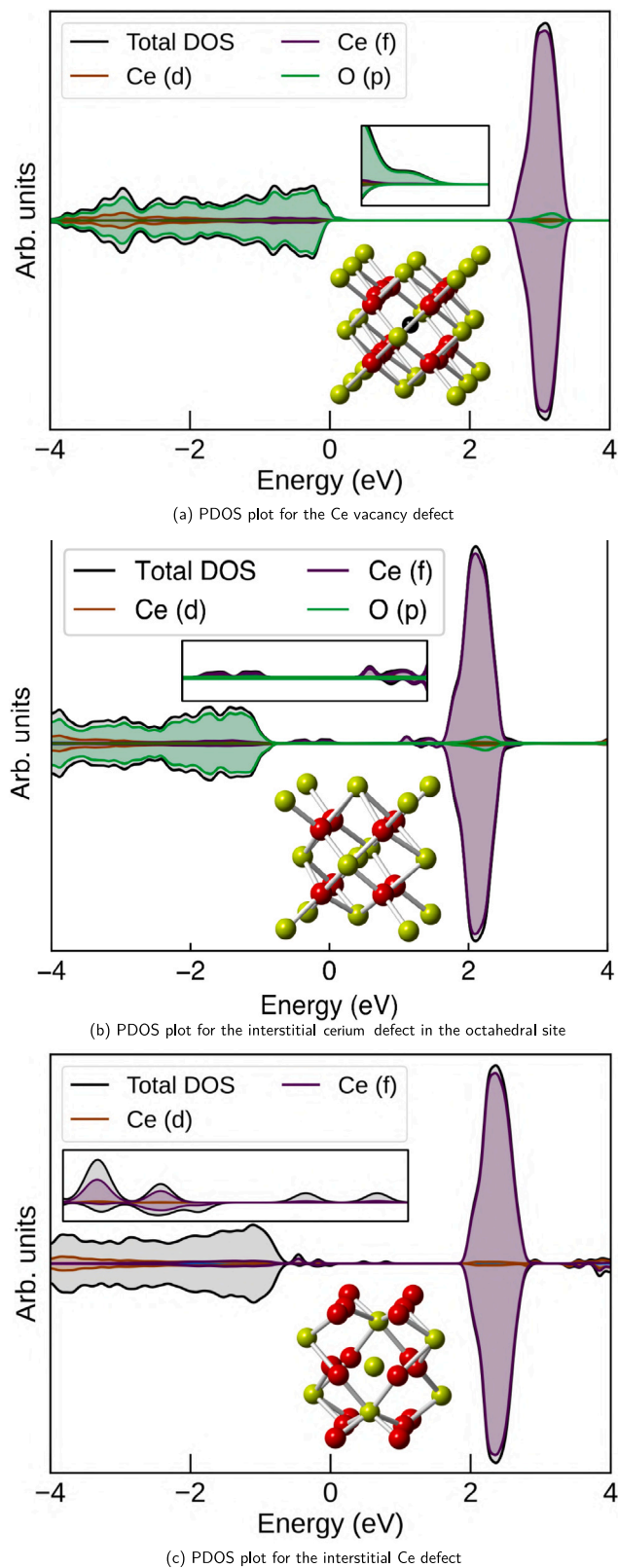
(a) PDOS plot for the Ce vacancy defect

(b) PDOS plot for the interstitial cerium defect in the octahedral site

(c) PDOS plot for the interstitial Ce defect

Fig. 2. Local structure around the (a) cerium vacancy, (b) interstitial cerium (octahedral) and (c) interstitial cerium (oxygen edge) defects in ceria and their respective PDOS plots for the 96 atom simulation cell from ONETEP. The oxygen atoms are given in red, cerium atoms in yellow and the cerium vacancy in black.

lattice oxygen reduces to a maximum of 0.16 Å in the 1500 supercell. Similarly, creating a cerium vacancy distorts the first nearest neighbour oxygen atoms by 0.22 Å in the 96 atom supercell, and to 0.07 Å in the 1500 atom supercell.

Placing an oxygen in an interstitial site between two oxygen sites, we measure a maximum displacement of 0.40 Å (CASTEP) and 0.48 Å (ONETEP) in the 96 atom cell for the first nearest neighbour oxygen atoms. This distortion is measured at just 0.09 Å (CASTEP) and 0.10 Å (ONETEP) with the interstitial in the octahedral site, which diminishes further in the 1500 atom cell to 0.05 Å (ONETEP). For the cerium interstitial octahedral site, the first nearest neighbour oxygen sites are displaced by 0.07 Å (CASTEP) and 0.14 Å (ONETEP) is measured in the 96 atom cell which reduces to 0.07 Å in the 1500 atom supercell. Larger distortion of first nearest neighbour oxygen atoms to the defect are measured when placed along the oxygen edge, at a maximum of 0.67 Å (CASTEP) and 0.70 Å (ONETEP).

Two different oxygen interstitial species form with CASTEP and ONETEP, so we report their energies separately in Table 2. The defect energies we have determined are greater than that of the stable peroxide species reported by Keating et al. [47]. We measured the distance between the interstitial oxygen and the nearest lattice oxygen atom at 2.48 Å (CASTEP) and 2.38 Å (ONETEP) when placed in an octahedral site. When placed between lattice oxygen sites, the separation reduces to 1.77 Å (CASTEP) and 1.87 Å (ONETEP). In both interstitial positions our O–O separation is measured to be greater than the 1.45 Å bond length reported for the peroxide species [101]. However, placing the interstitial approximately 1.0 Å from an oxygen lattice site, along the $\langle 111 \rangle$ direction, the peroxide species was formed. We measured the O–O bond length for the peroxide at 1.44 Å, which is close to the experimentally reported bond length.

For the cerium interstitial species we also find two different species forming. Depending on the position of the interstitial cerium, it is possible to localise three or four electrons on neighbouring cerium lattice atoms. The large difference in formation energies arise from the distortion of the neighbouring atoms, which is much more pronounced when the cerium is placed between two lattice oxygen sites. Similar distortions are found for the 96 atom simulation cell with ONETEP, however all four electrons are localised onto cerium lattice atoms for both interstitial positions. Expanding the simulation cell we find alternating electronic states with the cerium interstitial in the octahedral site.

3.3.2. Frenkel defect formation

The oxygen Frenkel (OF) defect were introduced by creating a vacancy on an oxygen lattice site and placing an oxygen in an interstitial position. Figure 12 in the supplementary material illustrates the positions of the interstitial oxygen atoms placed at increasing separation from the vacant site (black), along the $\langle 100 \rangle$ (blue), $\langle 110 \rangle$ (green) and $\langle 111 \rangle$ (purple) directions. The oxygen Frenkel defect formation process may be represented by the Kröger-Vink notation,

$$O_O^x \rightarrow V_O^{\bullet\bullet} + O_i'' \tag{14}$$

The 96 atom supercell imposes a limit on the number of available oxygen Frenkel defect configurations that can be investigated. Expanding the optimised simulation cell to 768 atoms in size allowed the placement of the interstitial oxygen further from the oxygen vacancy. Increasing the separation between the interstitial oxygen atom and the vacancy serves to reduce the interaction between the two sites within the cell. To avoid recombination, we find that placing the interstitial oxygen atom at least one interstitial site away from the vacancy is sufficient separation. In some cases then the interstitial combines with the vacancy during the calculation and these are denoted with the word 'Recombination' in Table 3.

Table 3 lists the oxygen Frenkel defect formation energies along different directions in the simulation cell, for increasing separations from the oxygen vacancy. Our formation energies are close to reported

Table 3
Oxygen Frenkel (OF) defect formation energies, per defect along the ⟨100⟩, ⟨110⟩ and ⟨111⟩ directions and comparison to computational literature.

Defect	Seperation (Å)	CASTEP (eV)	ONETEP (eV)		Literature (eV)	
		96 atom	96 atom	768 atom	OF (96 atom)	OF$_\infty$ (96 atom)
OF$_\infty$	–	2.79	2.38	2.65		
OF⟨100⟩	4.13	Recombination	Recombination	Recombination	1.95,	2.07,[b]
	6.88	1.23	1.61	2.03	2.01 ⟨111⟩,	2.02,[c]
	9.63	–	–	2.02	1.28 (5.88 Å),	2.12,[d]
OF⟨110⟩	5.18	1.99	1.71	1.59	1.33 (7.01 Å)	2.24,[f]
	9.72	1.99	1.69	1.64		2.15[g]
	13.62	–	–	1.58		
OF⟨111⟩	11.92	1.91	1.68	1.61		
	21.45	–	–	2.00		

[a] Ref. [47]. [b]Ref. [48]. [c]Ref. [28]. [d]Ref. [42]. [e]Ref. [102]. [f]Ref. [88] (QM/MM PBE0). [g]Ref. [88] (M-L).

values in the literature. Depending on the direction and separation from the vacancy, our energies are lower compared to the literature energies calculated at infinite dilution. Placing a vacancy and interstitial defect within the same simulation cell leads to a favourable stabilising interaction between them: which serves to lower the overall energy of the system when compared to the sum of the isolated defects [48].

For the OF⟨100⟩ direction we find that a separation of 4.13 Å is not sufficiently large enough to form a stable oxygen Frenkel defect. Keating et al. suggests that a separation of 7.17 Å leads to a stable oxygen Frenkel defect [47], although we find that 5.18 Å for the OF⟨110⟩ is sufficient. The minimal separation we found is closer to the prediction of the M-L model used by Catlow et al. at 5.88 Å. The chemical environment in which the interstitial oxygen resides also impacts the Frenkel energies. The interstitial oxygen occupies an octahedral site in the OF⟨111⟩, whereas in the OF⟨100⟩ and OF⟨110⟩ it sits close to oxygen lattice sites. The formation energy for the OF⟨111⟩ at a separation of 21.45 Å is comparable to that of the energies of the OF⟨100⟩, where the nearest neighbour oxygen atoms shift to accommodate the interstitial O. Whereas the energy of OF⟨111⟩ at 11.92 Å is lowered by the stronger interaction between the vacancy and interstitial oxygen.

The cerium Frenkel (CeF) defect are created in a similar manner to the oxygen Frenkel defects. Figure 13 in the supplementary material shows the fixed cerium vacancy position in the simulation cell. The interstitial cerium is placed at increasing separation from the vacant site (black), along the ⟨100⟩ (blue), ⟨110⟩ (green) and ⟨111⟩ (purple) directions. The cerium Frenkel defect formation process may be represented by,

$$Ce_{Ce}^x \rightarrow V_{Ce}'''' + Ce_i^{\bullet\bullet\bullet\bullet} \qquad (15)$$

The 96 atom supercell also imposes a limit on the number of available cerium Frenkel defect configurations that can be investigated, these are listed in Table 4. Fewer positions are available to create the cerium Frenkel defect, whilst minimising the interaction between periodic images and recombination. We find that placing the interstitial in the CeF⟨111⟩, at 4.77 Å from the vacancy is adequate to form a stable cerium Frenkel defect. Residing within the cerium sub-lattice, the interstitial positions in the CeF⟨100⟩ and CeF⟨111⟩ defects have an identical environment. In the CeF⟨110⟩, the cerium interstitial occupy positions between the tetrahedral oxygen in the lattice.

As noted with the oxygen Frenkel defects, our calculations produce smaller cerium Frenkel defect energies compared to the literature (Table 4). Like the oxygen Frenkel defects, this is due to the favourable interaction between the cerium vacancy and interstitial site. The literature cerium Frenkel defect formation energies derived from infinite dilution, where the vacancy and interstitial sites do not interact. This is also how many of the oxygen Frenkel formation energies listed in Table 3 have been previously reported. Our Frenkel formation energies

for cerium are comparable to the limited available literature, where we found greater deviation for the Frenkel energies calculated at infinite dilution. The large energy of the cerium vacancy formation we calculated and oscillating energies for the interstitial cerium contribute to the varying Frenkel energies at infinite dilution.

3.3.3. Schottky defect formation

The Schottky defects in Figure 14 of the supplementary material are introduced by removing one formula unit of CeO$_2$, which leaves one cerium and two oxygen vacancies. Three Schottky defect configurations are possible depending on the positions of the oxygen vacancies around the cerium vacancy. Keeping the position of one oxygen vacancy fixed, we can created the 2nd oxygen vacancy along the ⟨100⟩, ⟨110⟩ and ⟨111⟩ directions. The Schottky formation process is summarised by,

$$Ce_{Ce}^x + 2O_O^x \rightarrow V_{Ce}'''' + 2V_O^{\bullet\bullet} \qquad (16)$$

where removing the formula unit of CeO$_2$ leaves oppositely charged vacancies on the cerium and oxygen lattice sites.

Our bound Schottky defect formation energies given in Table 5 and Figure 11 are in the range of 1.0 eV to 1.8 eV per defect. At a 96 atom the simulation size, the Schottky defect energy along the ⟨100⟩ direction is predicted to be the most favourable; at larger simulation sizes the Schottky defect along the ⟨111⟩ becomes the most favourable. The least favourable Schottky defect is along the ⟨100⟩ direction, and this is true for all simulation sizes. This trend is in agreement with the available literature, with our energies falling close to the reported energy range. The formation energies reported by De Souza et al. [48] and Nakayama et al. [28] are calculated at infinite dilution, with no interactions between the vacancies forming the Schottky defect. We also found that our Schottky energies at infinite dilution are also larger than bound Schottky formation energies, and in good agreement with QM/MM results obtained by Catlow et al.

The bent geometry of the Schottky defects in the ⟨100⟩ and ⟨110⟩ directions leads to an effective dipole moment. Where the positive charge on the cerium cation does not align with that of the negative charge on the each of the oxygen anions. Whereas Schottky defect in ⟨111⟩ direction has no dipole moment due to the symmetry of its linear geometry. The investigation by Burr et al. demonstrates that the electrostatic interactions alone cannot account for the finite size effects [60]. In the 96 atom cell, artificial restoring forces from the periodic boundary conditions (PBC) suppress the atomic relaxation around the defect, raising the energy of Schottky defect along the ⟨111⟩ direction compared to the ⟨110⟩ direction.

Increasing the simulation size to 324 atoms and larger, we find that the energetic ordering changes to favour Schottky defect along ⟨111⟩ over the ⟨110⟩ direction for a given supercell size. The work by Burr et al. showed the same ordering of the Schottky defects for the larger relaxed supercell [60]. Their reported Schotthy defect energies for the ⟨100⟩ and ⟨111⟩ directions tend towards a converged energy

Table 4

Cerium Frenkel (CeF) defect formation energies, per defect along the ⟨100⟩, ⟨110⟩ and ⟨111⟩ directions and comparison to the computational literature.

Defect	Separation (Å)	CASTEP (eV)	ONETEP (eV)		Literature (eV)	
		96 atom	96 atom	768 atom	CeF (96 atom)	CeF$_\infty$ (96 atom)
CeF$_\infty$	–	7.72	7.10	8.69		
CeF⟨100⟩	2.75	Recombination	Recombination	Recombination		
	8.26	–	–	5.29		
CeF⟨110⟩	6.07	Recombination	Recombination	Recombination	5.51[a] ⟨111⟩	6.23,[b] 7.36[c]
	9.73	–	–	5.82		
	13.62	–	–	5.36		
CeF⟨111⟩	4.77	5.10	5.00	5.32		
	14.30	–	–	5.87		

[a]Ref. [102]. [b]Ref. [48]. [c]Ref. [28].

Table 5

Schottky (S) defect formation energies along the ⟨100⟩, ⟨110⟩ and⟨111⟩ direction and comparison to the computational literature. The values taken from Ref. [60] are an approximation from the formation energies plotted as a function of simulation cell size.

Defect	CASTEP (eV)	ONETEP (eV)				Literature (eV)			
	96 atom	96 atom	324 atom	768 atom	1500 atom	S (96 atom)	S (324 atom)	S (768 atom)	S$_\infty$ (96 atom)
S$_\infty$	3.77	3.06	3.88	3.06	3.93	–	–	–	2.29,[d] 3.59,[e] 3.08[g]
S⟨100⟩	1.36	1.24	1.58	1.38	1.84	1.83,[a] ~1.43,[b] 1.64,[f] 1.95[h]	~1.41[b]	~1.42[b]	–
S⟨110⟩	1.12	0.99	1.47	1.06	1.71	1.64,[a] ~1.23,[b] 1.19,[c] 1.41,[f] 1.74[h]	~1.24[b]	~1.26[b]	–
S⟨111⟩	1.22	1.08	1.40	0.98	1.30	1.67,[a] ~1.30,[b] 1.49,[f] 1.73[h]	~1.23[b]	~1.24[b]	–

[a]Ref. [49]. [b]Ref. [60]. [c]Ref. [47]. [d]Ref. [48]. [e]Ref. [28]. [f]Ref. [102]. [g]Ref. [88] (QM/MM PBE0). [h]Ref. [88] (M-L).

with increasing simulation cell size. However, we found that our defect energies fluctuate between odd and even simulation sizes (2x2x2 vs. 3x3x3 etc.). Burr et al. found varying behaviour of defect energies with increasing simulation size for several FCC materials. Castleton et al. have also shown an increase in formation energy of the Schottky defects with increasing simulation size [97].

4. Conclusions

In this work, we have calculated the bulk properties and intrinsic defects in ceria, using both conventional and linear-scaling DFT methods. Our selection of the Hubbard parameter, U at 5.0 eV, strikes a good balance between the lattice parameter of 5.50 Å and band gap of 2.70 eV for the material. We determined the unique elastic properties of ceria and moduli and shown that they compare well to the literature values. Our calculated bulk properties are in close agreement with the reported range from previous computational work. The differences from the experimentally obtained properties are due to our choice of DFT parameters and not accounting for temperature and volume effects.

We have studied point, Frenkel and Schottky defects with simulation cells up to 1500 atoms in size which are an improved approximation of bulk ceria. Increasing the simulation size in ONETEP, we found that the vacancy and interstitial defect energies fluctuate. We cannot definitively identify the cause of this behaviour but several possibilities exist. The most likely is a symmetry explanation noting that this has been observed before. In addition, there may also be an electronic effect arising from distortions around the defect. These become weaker as the simulation cell size increases.

With ONETEP we were able to find the stable ground state of the oxygen vacancy defect, reducing two nearest neighbour cerium sites. We found that the cerium vacancy was the least favourable point defect, with holes localised across several nearest neighbour oxygen sites. Our cerium vacancy energies are calculated to within a small range from 13.58 eV to 14.67 eV, whereas the literature energies have a wider range from 4.94 eV to 16.59 eV. With increasing simulation cell size, we measured the distortion of the first nearest neighbours oxygen sites to the vacancy reduce from a maximum of 0.31 Å to 0.16 Å for oxygen and 0.22 Å to 0.07 Å for cerium.

We also formed different charged states for the oxygen and cerium interstitial species within CASTEP and ONETEP, by changing the position of the defect. The peroxide species was found to be the most stable interstitial species, formed by offsetting the interstitial oxygen from the octahedral site, approximately 1.0 Å from the lattice oxygen atom. Whereas placing the cerium in the octahedral interstitial site was found to be most stable cerium point defect, minimising the distortion of the lattice. The most stable cerium point defect arises from placing it in the octahedral interstitial site.

We also investigated how the simulation size impacts the energetic orderings of the bound Schottky defects. At the 96 atom supercell size, Schottky defect in the ⟨110⟩ direction is predicted to be the most favourable, which is due to artificial restoring forces. At the larger simulation sizes the Schottky defect in the ⟨111⟩ direction becomes more favourable than the ⟨110⟩ direction. Increasing the simulation cell size, we also explored several Frenkel defect configurations, aiming to minimise the interaction between the vacancy and interstitial site and their periodic images. We determined the minimal separation between the vacancy and interstitial site to form a stable defect. Our calculations suggest that a distance between the vacancy and interstitial sites of 5.18 Å along the ⟨110⟩ direction for the oxygen Frenkel and 4.77 Å along the ⟨111⟩ for the cerium Frenkel is sufficient.

Our investigation of ceria provides a foundation for more representative simulations of other industrially relevant materials. We can use our understanding of intrinsic defects that we have developed in this work to apply this to the PuO_2. Chemically similar to ceria, PuO_2 has a more complex electronic structure, with some of its $5f$-states occupied which will need to be considered.

CRediT authorship contribution statement

Nabeel Anwar: Investigation, Writing – original draft, Writing – review & editing. **Robert M. Harker:** Conceptualization, Supervision, Writing – review & editing. **Mark T. Storr:** Conceptualization, Supervision, Writing – review & editing. **Marco Molinari:** Conceptualization, Supervision, Writing – review & editing. **Chris-Kriton Skylaris:** Conceptualization, Supervision, Writing – original draft, Writing – review & editing.

Declaration of competing interest

The authors declare that they have no known competing financial interests or personal relationships that could have appeared to influence the work reported in this paper.

Data availability

Data will be made available on request.

Appendix A. Supplementary data

Supplementary material related to this article can be found online at https://doi.org/10.1016/j.commatsci.2023.112396. Raw data is available at https://doi.org/10.17632/mxvwntb5wy.1 containing the input files including the calculation parameters and the output files with the optimised structures.

References

[1] W. Deng, C. Carpenter, N. Yi, M. Flytzani-Stephanopoulos, Top. Catal. 44 (2007) 199–209.
[2] A.J. Jacobson, Chem. Mater. 22 (2010) 660–674.
[3] A. Khodadadia, S.S. Mohajerzadehb, Y. Mortazavia, A.M. Miri, Sensors Actuators B 80 (2001) 267–271.
[4] K. Krishna, A. Bueno-López, M. Makkee, J.A. Moulijn, Top. Catal. 42 (2007) 221–228.
[5] J.G. Nunan, M.J. Cohn, J.T. Dormer, Catal. Today 14 (1992) 277–291.
[6] K. Zhou, X. Wang, X. Sun, Q. Peng, Y. Li, J. Catal. 229 (2005) 206–212.
[7] R. Si, M. Flytzani-Stephanopoulos, Angew. Chem. 120 (2008) 2926–2929.
[8] P. Panagiotopoulou, J. Papavasiliou, G. Avgouropoulos, T. Ioannides, D. Kondarides, Chem. Eng. J. 134 (2007) 16–22.
[9] M.F. Camellone, S. Fabris, J. Am. Chem. Soc. 131 (2009) 10473–10483.
[10] M.V. Ganduglia-Pirovano, C. Popa, J. Sauer, H. Abbott, A. Uhl, M. Baron, D. Stacchiola, O. Bondarchuk, S. Shaikhutdinov, H.-J. Freund, J. Am. Chem. Soc. 132 (2010) 2345–2349.
[11] S. Basu, P.S. Devi, H. Maiti, J. Mater. Res. 19 (2004) 3162–3171.
[12] M. Henderson, C. Perkins, M. Engelhard, S. Thevuthasan, C. Peden, Surf. Sci. 526 (2003) 1–18.
[13] Z. Yang, T.K. Woo, J. Chem. Phys. 120 (2004) 7741–7749.
[14] D.A. Andersson, Appl. Phys. Lett. 90 (2007) 031909.
[15] E.B. Lavik, I. Kosacki, H.L. Tuller, Y.-M. Chiang, J.Y. Ying, J. Electroceram. 1 (1997) 7–14.
[16] M. Nolan, J.E. Fearon, G.W. Watson, Solid State Ion. 117 (2006) 3069–3074.
[17] H. Inaba, H. Tagawa, Solid State Ion. 83 (1996) 1–16.
[18] D.A. Andersson, S.I. Simak, N.V. Skorodumova, I.A. Abrikosov, B. Johansson, Proc. Natl. Acad. Sci. 103 (2006) 3518–3521.
[19] Y.-P. Fu, C.-W. Tseng, P.-C. Peng, J. Eur. Ceram. Soc. 28 (2008) 85–90.
[20] S. Kuharuangrong, J. Power Sources 171 (2007) 506–510.
[21] B. Rambabu, S. Ghosh, H. Jena, J. Mater. Sci. 41 (2006) 7530–7536.
[22] S. Sen, H.J. Avila-Paredes, S. Kim, J. Mater. Chem. 18 (2008) 3915–3917.
[23] B. Zhu, X. Liu, Z. Zhu, R. Ljungberg, Int. J. Hydrog. Energy 33 (2008) 3385–3392.
[24] S. Zha, C. Xia, G. Meng, J. Power Sources 115 (2002) 44–48.
[25] X. Sha, Z. Lu, X. Huang, J. Miao, Z. Ding, X. Xin, W. Su, J. Alloys Compd. 428 (2007) 59–64.
[26] X. Guan, H. Zhou, Z. Liu, Y. Wang, J. Zhang, Mater. Res. Bull. 43 (2008) 1046–1054.
[27] C.H. Cheng, S.F. Lee, C.W. Hong, J. Electrochem. Soc. 154 (2007) E158.
[28] M. Nakayama, M. Martin, Phys. Chem. Chem. Phys. 11 (2009) 3241–3249.
[29] D.J.L. Brett, A. Atkinson, N.P. Brandon, S.J. Skinner, Chem. Soc. Rev. 37 (2008) 1568–1578.
[30] G. Magesh, B. Viswanathan, R.P. Viswanath, T.K.V. Varadarajan, Indian J. Chem. A 46A (2009) 480–488.
[31] S. Sathyamurthy, K.J. Leonard, R.T. Dabestani, M.P. Paranthaman, Nanotechnology 16 (2005) 1960–1964.
[32] S. Debnath, M.R. Islam, M.S.R. Khan, Bull. Mater. Sci. 30 (2007) 315–319.
[33] H. Matzke, Radiation Effects in Solids, Springer, Dordrecht, 2007, pp. 401–420, Chap. 14.
[34] D. Olander, J. Nucl. Mater. 389 (2009) 1–22.
[35] W. Huang, H. Chen, Physica B 449 (2014) 133–137.
[36] V. Kanchana, G. Vaitheeswaran, A. Svane, A. Delin, J. Phys.: Condens. Matter 18 (2006) 9615–9624.
[37] M.W.D. Cooper, M.J.D. Rushton, R.W. Grimes, J. Phys.: Condens. Matter 26 (2014) 105401.
[38] J.T. Pegg, X. Aparicio-Anglès, M.T. Storr, N.H. de Leeuw, J. Nucl. Mater. 492 (2017) 269–278.
[39] S.L. Dudarev, Annu. Rev. Mater. Res. 43 (2013) 35–61.
[40] S.L. Dudarev, P.M. Derlet, C.H. Woo, Nucl. Instrum. Methods Phys. Res. B 256 (2007) 253–259.
[41] Y. Satoh, H. Matsui, T. Hamaoka, Phys. Rev. B 77 (2008) 094135.
[42] S. Grieshammer, Phys. Chem. Chem. Phys. 20 (2018) 19792–19799.
[43] D. Staicu, T. Wiss, V.V. Rondinella, J.P. Hiernaut, R.J.M. Konings, C. Ronchi, J. Nucl. Mater. 397 (2010) 8–18.
[44] J.L.F.D. Silva, M.V. Ganduglia-Pirovano, J. Sauer, V. Bayer, G. Kresse, Phys. Rev. B 75 (2007) 045121.
[45] P.J. Hay, R.L. Martin, J. Uddin, G.E. Scuseria, J. Chem. Phys. 125 (2006) 034712.
[46] L. Brugnoli, A.M. Ferrari, B. Civalleri, A. Pedone, M.C. Menziani, J. Chem. Theory Comput. 14 (2018) 4914–4927.
[47] P.R.L. Keating, D.O. Scanlon, B.J. Morgan, N.M. Galea, G.W. Watson, J. Phys. Chem. C 116 (2012) 2443–2452.
[48] T. Zacherle, A. Schriever, R.A.D. Souza, M. Martin, Phys. Rev. B 87 (2013) 134104.
[49] L. Shi, E. Vathonne, V. Oison, M. Freyss, R. Hayn, Phys. Rev. B 94 (2016) 115132.
[50] C. Freysoldt, J. Neugebauer, C.G.V. de Walle, Phys. Rev. Lett. 102 (2009) 016402.
[51] C. Freysoldt, B. Grabowski, T. Hickel, J. Neugebauer, G. Kresse, A. Janotti, C.G.V. de Walle, Rev. Modern Phys. 86 (2014) 253–305.
[52] S. Lany, A. Zunger, Phys. Rev. B 78 (2008) 235104.
[53] G. Makov, M.C. Payne, Phys. Rev. B 51 (1995) 4014–4022.
[54] C. Freysoldt, J. Neugebauer, C.G.V. de Walle, Phys. Status Solidi b 248 (2011) 1067–1076.
[55] J.C.A. Prentice, J. Aarons, J.C. Womack, A.E.A. Allen, L. Andrinopoulos, L. Anton, R.A. Bell, A. Bhandari, G.A. Bramley, R.J. Charlton, R.J. Clements, D.J. Cole, G. Constantinescu, F. Corsetti, S.M.-M. Dubois, K.K.B. Duff, J.M. Escartín, A. Greco, Q. Hill, L.P. Lee, E. Linscott, D.D. O'Regan, M.J.S. Phipps, L.E. Ratcliff, Á.R. Serrano, E.W. Tait, G. Teobaldi, V. Vitale, N. Yeung, T.J. Zuehlsdorff, J. Dziedzic, P.D. Haynes, N.D.M. Hine, A.A. Mostofi, M.C. Payne, C.-K. Skylaris, J. Chem. Phys. 152 (2020) 174111.
[56] W. Kohn, Phys. Rev. Lett. 76 (1996) 3168–3171.
[57] E. Prodan, W. Kohn, Proc. Natl. Acad. Sci. 102 (2005) 11635–11638.
[58] C.-K. Skylaris, A.A. Mostofi, P.D. Haynes, O. Diéguez, M.C. Payne, Phys. Rev. B 66 (2002) 035119.
[59] C.-K. Skylaris, P.D. Haynes, A.A. Mostofi, M.C. Payne, J. Chem. Phys. 122 (2005) 084119.
[60] P.A. Burr, M.W.D. Cooper, Phys. Rev. B 96 (2017) 094107.
[61] K. Govers, S. Lemehov, M. Hou, M. Verwerft, J. Nucl. Mater. 366 (2007) 161–177.
[62] M.W.D. Cooper, M.J.D. Rushton, R.W. Grimes, J. Phys.: Condens. Matter 26 (2014) 105401.
[63] S.J. Clark, M.D. Segall, C.J. Pickard, P.J. Hasnip, M.I.J. Probert, K. Refson, M.C. Payne, Z. Kristallogr. 220 (2005) 567–570.
[64] J.P. Perdew, K. Burke, M. Ernzerhof, Phys. Rev. Lett. 77 (1996) 3865–3868.
[65] H.J. Monkhorst, J.D. Pack, Phys. Rev. B 13 (1976) 5188–5192.
[66] M. Cococcioni, S. de Gironcoli, Phys. Rev. B 71 (2005) 035105.
[67] S.L. Dudarev, G.A. Botton, S.Y. Savrasov, C.J. Humphreys, A.P. Sutton, Phys. Rev. B 57 (1998) 1505–1509.
[68] C.W.M. Castleton, J. Kullgren, K. Hermansson, J. Chem. Phys. 127 (2007) 244704.
[69] M. Nolan, S.C. Parker, G.W. Watson, Surf. Sci. 595 (2005) 223–232.
[70] M. Nolan, S. Grigoleit, D.C. Sayle, S.C. Parker, G.W. Watson, Surf. Sci. 576 (2005) 217–229.
[71] J. Paier, C. Penschke, J. Sauer, Chem. Rev. 113 (2013) 3949–3985.
[72] C. Loschen, J. Carrasco, K.M. Neyman, F. Illas, Phys. Rev. B 75 (2007) 035115.
[73] A.I. Liechtenstein, V.I. Anisimov, J. Zaanen, Phys. Rev. B 52 (1995) R5467.
[74] G. Jomard, B. Amadon, F. Bottin, M. Torrent, Phys. Rev. B 78 (2008) 075125.
[75] B. Amadon, F. Jollet, M. Torrent, Phys. Rev. B 77 (2008) 155104.
[76] J.P. Allen, G.W. Watson, Phys. Chem. Chem. Phys. 16 (2014) 21016–21031.
[77] P.D. Haynes, A.A. Mostofi, C.-K. Skylaris, M.C. Payne, J. Phys.: Conf. Ser. 26 (2006) 143–148.
[78] S.B. Zhang, J.E. Northrup, Phys. Rev. Lett. 67 (1991) 2339–2342.
[79] G.A. Baraff, M. Schlüter, Phys. Rev. Lett. 55 (1985) 1327–1330.
[80] Y.Z. Zhu, G.D. Chen, H. Ye, A. Walsh, C.Y. Moon, S.-H. Wei, Phys. Rev. B 77 (2008) 245209.
[81] D.R. Mullins, S.H. Overbury, D.R. Huntley, Surf. Sci. 409 (1998) 307–319.

[82] E. Wuilloud, B. Delley, W.-D. Schneider, Y. Baer, Phys. Rev. Lett. 53 (1984) 202–205.

[83] A. Nakajima, A. Yoshihara, M. Ishigame, Phys. Rev. B 50 (1994) 13297.

[84] K. Clausen, W. Hayes, J.E. Macdonald, R. Osborn, P.G. Schnabel, M.T. Hutchings, A. Magerl, J. Chem. Soc. Faraday Trans. 2 83 (1987) 1109–1112.

[85] S. Sathyamurthy, K.J. Leonard, R.T. Dabestani, M.P. Paranthaman, Nanotechnology 16 (2005) 1960–1964.

[86] A. Boudjemline, L. Louail, M.M. Islam, B. Diawara, Comput. Mater. Sci. 50 (2011) 2280–2286.

[87] L. Gerward, J.S. Olsen, L. Petit, G. Vaitheeswaran, V. Kanchana, A. Svane, J. Alloys Compd. 400 (2005) 56–61.

[88] X. Zhang, L. Zhu, Q. Hou, J. Guan, Y. Lu, T.W. Keal, J. Buckeridge, C.R.A. Catlow, A.A. Sokol, Chem. Mater. 35 (2023) 207–227.

[89] Elastic constants, 2022, https://github.com/andreww/elastic-constants, (accessed September 2022).

[90] R. Hill, Proc. Phys. Soc. A 65 (1952) 349–354.

[91] M. Born, Math. Proc. Cambridge Philos. Soc. 36 (1940) 160–172.

[92] D.D. O'Regan, N.D.M. Hine, M.C. Payne, A.A. Mostofi, Phys. Rev. B 82 (2010) 081102.

[93] D.E.P. Vanpoucke, P. Bultinck, S. Cottenier, V.V. Speybroeck, I.V. Driessche, J. Mater. Chem. A 2 (2014) 13723–13737.

[94] A.M. Ganose, A.J. Jackson, D.O. Scanlon, J. Open Source Softw. 3 (2018) 1–3.

[95] D. Mullins, P. Radulovic, S. Overbury, Surf. Sci. 429 (1999) 186–198.

[96] B. Huang, R. Gillen, J. Robertson, J. Phys. Chem. C 118 (2014) 24248–24256.

[97] C.W.M. Castleton, S. Mirbt, Physica B 340–342 (2003) 407–411.

[98] C.W.M. Castleton, S. Mirbt, Phys. Rev. B 70 (2004) 195202.

[99] C.W.M. Castleton, A. Höglund, S. Mirbt, Modelling Simul. Mater. Sci. Eng. 17 (2009) 084003.

[100] X. Luo, R.M. Martin, Phys. Rev. B 72 (2005) 035212.

[101] C.J. Cramer, W.B. Tolman, K.H. Theopold, A.L. Rheingold, Proc. Natl. Acad. Sci. USA 100 (2003) 3635–3640.

[102] T. Smith, S. Moxon, J.S. Tse, J.M. Skelton, D.J. Cooke, L.J. Gillie, E.L. da Silva, R.M. Harker, M.T. Storr, S.C. Parker, M. Molinari, J. Phys. Energy 5 (2023) 025004.